Chemical Engineering Science 284 (2024) 119479

Contents lists available at ScienceDirect

Chemical Engineering Science

journal homepage: www.elsevier.com/locate/ces

Hanging a droplet with minimized intervention

Xiaofang Zhang [a], Oluwafemi Ayodele George [b], Hong Zhu [a], Zhe Zhang [a], Haoyu Zhuo [a], Nan Fu [a], Meng Wai Woo [c], Xiao Dong Chen [a], Jie Xiao [a,*]

[a] Particle Engineering Laboratory, Suzhou Key Laboratory of Green Chemical Engineering, School of Chemical and Environmental Engineering, College of Chemistry, Chemical Engineering and Materials Science, Soochow University, Suzhou 215123 China
[b] Department of Systems Engineering, Faculty of Engineering, University of Lagos, Akoka, Nigeria
[c] Department of Chemical and Materials Engineering, The University of Auckland, Auckland 1023, New Zealand

ARTICLE INFO

Keywords:
Droplet hanging
Suspender design
Contact angle
Minimum intervention
Numerical simulation

ABSTRACT

Single droplet drying (SDD) by glass filament apparatus is a powerful tool for tracking droplet drying kinetics. However, the level and influence of intrusion of glass suspender into droplet have not been fully elucidated. In this work, the hanging processes of droplets by suspenders are numerically simulated by the volume of fluid (VOF) method, aimed at improved design of suspenders that can offer reduced suspender-droplet contact and increased droplet sphericity. Furthermore, the hanging simulation has been extended to small-sized droplets similar to those in spray drying operation which are too small to be addressed by the existing SDD technique. A comparison diagram of droplet suspension states at two scales has been constructed, which provides different suspension states of droplets as determined by the size of the suspender and the contact angle. The quantitative results can guide the design of minimal-intervention suspenders for droplets with specific properties.

1. Introduction

Droplet drying is a common phenomenon in not only our daily life but also a wide range of industrial productions. Many important food and pharmaceutical products are in the form of dry powders that should be made through drying of atomized droplets. Thus, understanding the drying process of droplets is critical for ensuring powder product quality. There are many studies on droplet drying kinetics, widely involved in physics, chemistry, material science, and medicine. The investigation of the evaporation process of droplets containing non-volatile solutes on substrate surfaces has contributed to the understanding of solute deposition patterns (Deegan et al., 1997; Larson, 2017). The self-assembly of particles dispersed in droplets driven by the evaporation provides a new method for making micro- and nanoparticles, which has been widely used in the preparation of functional materials (Zang et al., 2019). Atomized droplets in a spray cooling system can rapidly absorb heat from the surrounding air and effectively regulate the local thermal environment, which has been widely used for fire detection and explosion prevention in safety science (Wen et al., 2019), farming (Liu and Kang, 2006), and urban thermal environment improvement (Meng et al., 2022). By investigating the evaporation characteristics of aerosols, one can construct mathematical models for virus transmission (Chaudhuri et al., 2020). It can help the design of personal protective equipment in response to COVID-19 (Bhardwaj and Agrawal, 2020), and provide data for the scientific specification of social distances (Rosti et al., 2020). Spray drying is an effective approach to convert liquid into solid powders and has been widely used in food (Piñón-Balderrama et al., 2020), pharmaceuticals (Baumann et al., 2021), and materials (Zandona et al., 2021) industries. In spray drying, the size, morphology, and surface structure of the solid particles formed under different droplet drying conditions are analyzed by scanning electron microscopy and other techniques for the study of the droplet drying mechanism (Wu et al., 2011; Littringer et al., 2013; Both et al., 2020). The rapid drying kinetics in spray drying makes it difficult to sample and record the physical phenomena occurring in each droplet during the intermediate stages of drying (Fu et al., 2012). The main drawback of spray drying experiments is the inability to directly monitor the drying kinetics of single droplets and their collision behavior, which complicates the study of the process in spray drying towers. For a better understanding of the droplet drying process and its influence on particle formation, single droplet drying (SDD) techniques can be used to monitor the drying of a single droplet under a well-controlled drying environment. In single droplet drying, to keep the droplet at a fixed location is a crucial first step, which requires a droplet support system. There are two types of droplet support systems,

* Corresponding author.
E-mail address: jie.xiao@suda.edu.cn (J. Xiao).

https://doi.org/10.1016/j.ces.2023.119479
Received 29 May 2023; Received in revised form 22 October 2023; Accepted 4 November 2023
Available online 7 November 2023

Table 1
Comparisons of supporting schemes for a single droplet.

Droplet supporting methods	Non-intrusive methods Acoustic levitation	Aerodynamic levitation	Electrodynamic levitation	Intrusive methods Hanging methods	Horizontal support methods
Schematic		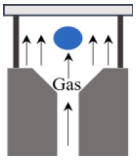	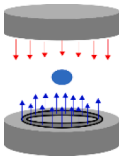	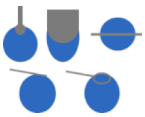	
Droplet size	300 μm-1 mm	>1 mm	10 μm –100 μm	>500 μm	>150 μm
Droplet types	Dextrin droplet, nano silica water droplet, binary water/methanol droplet, binary water/ethanol droplet	Liquid alumina droplet, molten uranium dioxide droplet, binary uranium dioxide-zirconium compositions droplet	Aqueous sodium chloride solution droplets, hydrophilic silica droplets	Skim milk, whole milk, hypromellose phthalate droplet, lactose droplet	Nanofluid droplet, protein droplet, maltodextrin droplet
Pros	-Monitoring droplet mass and temperature history	-Similar to droplets in the spray drying chamber -Monitoring droplet mass and temperature history	-Monitoring droplet mass changes	-Monitoring droplet mass and temperature history, and morphology changes	-Monitoring droplet mass and shape changes
Cons	-Acoustic field force deforms droplets -Acoustic field greatly changes the heat and mass transfer rate of droplets	- Difficult to maintain stability of the droplet	–No monitoring of droplet temperature, and particle morphology evolution	-Suspender intrusion inside the droplet, affecting the mass and heat transfer -Suspender affects the droplet shape	-Support surface affects the heat and mass transfer -Support surface induces nucleation
References	(Groenewold et al., 2002; Al Zaitone et al., 2020; Saha et al., 2012; Yarin et al., 2002; Eijkelboom et al., 2022)	(Langstaff et al., 2013; Weber et al., 2016; de Souza Lima et al., 2020)	(Gregson et al., 2018; Archer et al., 2020)	(Charlesworth and Marshall Jr 1960; Lin and Chen, 2002; Fu et al., 2011; Su et al., 2020; Radhakrishnan et al., 2019; Volkov and Strizhak, 2021; de Souza Lima et al., 2020)	(Bansal et al., 2018; Both et al., 2019; Perdana et al., 2013)

i.e., non-intrusive and intrusive ones (Table 1). Non-intrusive systems do not need a substrate surface to get in touch with the droplet. Acoustic levitation (Groenewold et al., 2002; Al Zaitone et al., 2020; Saha et al., 2012; Yarin et al., 2002), aerodynamic levitation (Langstaff et al., 2013; Weber et al., 2016), and electrodynamic levitation (Gregson et al., 2018; Archer et al., 2020) are representative techniques. Intrusive systems, however, use intrusive substances to hold the droplet in place, such as glass filaments (Charlesworth and Marshall Jr 1960; Lin and Chen, 2002; Fu et al., 2011; Su et al., 2020), hydrophobic surfaces (Bansal et al., 2018; Both et al., 2019; Perdana et al., 2013), metallic wires (Vershinina et al., 2016), quartz wires (Raghavan and Mehta, 2015), needles and rods made of glass and steel (Radhakrishnan et al., 2019), and horizontally placed fibers or thermocouples (Rehman et al., 2016; Surendran et al., 2020; Rosli et al., 2021), etc.

Two major challenges have to be addressed to improve the current droplet support systems. The first one is to reduce the intervention from the support system, which may significantly affect droplet drying behavior. Even for a non-intrusive system, the acoustic field applied by the acoustic levitation affects the droplet shape as well as the rate of heat and mass transfer. In the intrusive system, the contact area between the suspender and the droplet affects heat, mass transfer, and morphological evolution. Several experimental studies have investigated the effects of the suspenders' shape and material on droplet drying (Radhakrishnan et al., 2019; Liu and Kang, 2006; Chauveau et al., 2011; Vershinina et al., 2016; Volkov and Strizhak, 2021). Chauveau et al. (2011) explored the effect of quartz fibers with different diameters on the evaporation rate of n-decane droplets and found that the vaporization rate of droplets increased with increasing fiber diameter. Vershinina et al. (2016) positioned fuel droplets on three substrate materials with different thermal conductivities, i.e., ceramic rods, thermocouples, and metal wires, to explore the effect of three different supports on the ignition behavior of coal-water slurry containing petrochemical droplets. Radhakrishnan et al. (2019) studied the effect of needle and rod suspenders made of glass and steel with different thermal conductivities on the heat transfer and evaporation rates of ethanol and water, which decreased with decreasing suspender diameter. Volkov and Strizhak (2021) designed three different schemes of suspenders and investigated the effects of suspender material, suspender diameter, and suspender-droplet contact area on droplet heating and evaporation. The results showed that the increase of the suspender-droplet contact area decreased the evaporation time and accelerated the droplet evaporation process. The intrusive effects of the suspender have also been studied by numerical simulations (Shih and Megaridis, 1995; Ghata and Shaw, 2014; George et al., 2017; George et al., 2019). Ghata and Shaw (2014) established a multidimensional computational fluid dynamics (CFD) model to demonstrate the effect of different fiber diameters on droplet flow, evaporation rate, and droplet shape. They observed the increase in vapor mass fraction along the interface with increasing fiber diameter. George et al. (2017) used CFD methods to model single droplet drying and revealed that the heat transfer through the suspender increases with increasing glass knob diameter. George et al. (2019) further quantified the effect of heat conduction from the glass filament knob on the evaporation rate of droplets.

The second challenge is the mismatch between the size of the droplet in a single droplet drying experiment and the size of droplets of interests. As shown in Table 1, droplet sizes in single droplet drying experiments are typically larger than 100 μm. Note that, liquid droplets generated from industrial spray-drying atomizers usually range in size from 1 to 1000 μm (Wu et al., 2007; Filková and Mujumdar, 2020), and aerosols generated from the respiratory tract during exhalation activities such as breathing, talking, coughing and sneezing range in size from 0.1 μm-1000 μm (Mittal et al., 2020). Such a wide range of droplet size can be hardly covered by most currently available single droplet drying systems, especially for the smaller-sized droplets, e.g., 100 μm and below, which is the normal size of atomized droplets in an industrial spray dryer (Lin and Chen, 2002). Experimentally, hanging a droplet of less than 100 μm with negligible intervention from the support system is very challenging.

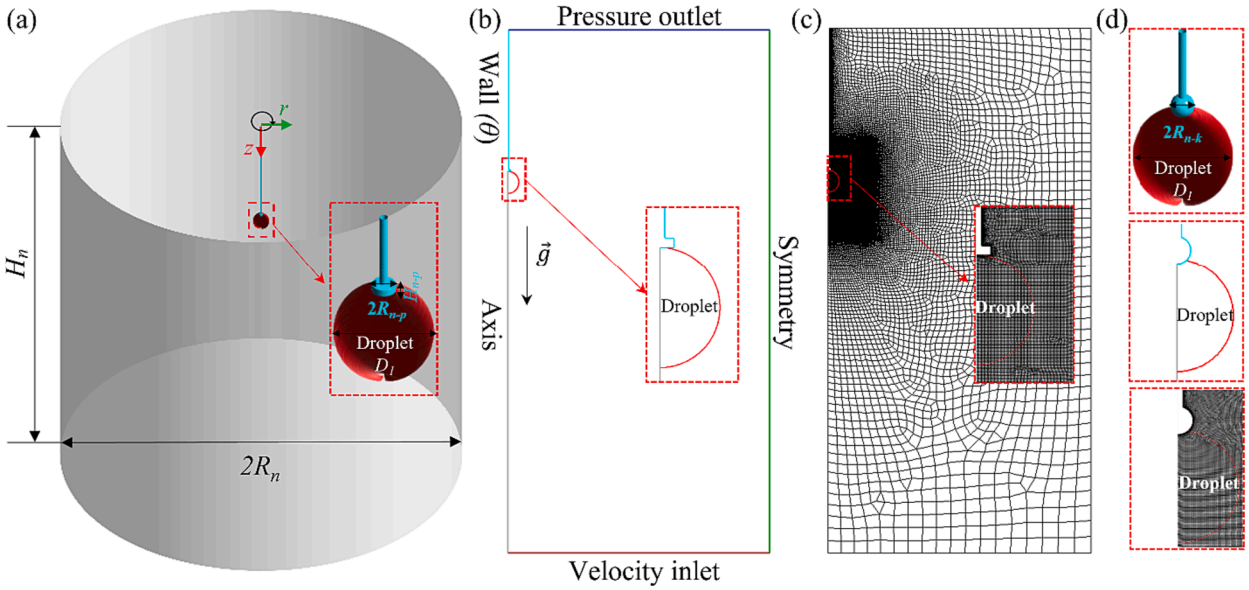

Fig. 1. Schematic diagrams of (a) simulation domain, (b) boundary conditions, (c) mesh for the system with a plate suspender, and (d) the knob model.

Table 2
Parameter settings for the base case models.

Parameters			Notation	Model values	References
Scale-normal model	Computational domain	Height	H_n	30 mm	(Lin and Chen, 2002)
		Radius	R_n	15 mm	
	Glass filament rod radius		$R_{n\text{-}f}$	0.05 mm	(Fu et al., 2011)
	Knob radius		$R_{n\text{-}k}$	0.15 mm	(Fu et al., 2011)
	Plate radius		$R_{n\text{-}p}$	0.15 mm	
	Plate thickness		$H_{n\text{-}p}$	0.10 mm	(Su et al., 2020)
Scale-down model	Computational domain	Height	H_d	2.42 mm	
		Radius	R_d	1.21 mm	
	Glass filament rod radius		$R_{d\text{-}f}$	0.004 mm	
	Plate radius		$R_{d\text{-}p}$	0.0121 mm	
	Plate thickness		$H_{d\text{-}p}$	0.0081 mm	

To achieve accurate measurements, an ideal support system should minimize its intervention on the droplet. Moreover, the single droplet used as a model droplet needs to match the droplet size in a real production application so that the results obtained with the single droplet drying system can be extended to a large-scale spray drying system involving numerous flying droplets.

The glass filament SDD technique has been frequently utilized as a powerful instrument to determine droplet drying kinetics. The glass filament is generally designed as a spherical shape with a diameter of 200 μm-300 μm (Fu et al., 2011). It was found that, in many cases, droplets tend to climb the suspender along the glass filament, which increases the intrusion of the filament into the droplets and affects the heat and mass transfer. By using an ultrathin rectangular plate with an edge length of about 550 μm-600 μm and a thickness of about 100 μm-120 μm instead of a coated glass knob suspender, the problem of droplet climbing could be avoided (Su et al., 2020). There is a growing interest in the design of an optimal suspender that can reduce the intrusive influence on the single droplet. The study is expected to be able to disclose the influence of the size, structure, and wettability of the material surface of the suspender on the droplet flow behavior during the droplet pendant process. In addition, glass filament SDD experiments usually use droplets with initial sizes of 500 μm −2000 μm (Charlesworth and Marshall Jr 1960; Lin and Chen, 2002; Fu et al., 2011). Current experimental technique is not capable of suspending smaller sized droplets, which are usually encountered in real situations such as spray-dried droplets as well as aerosol droplets.

For minimal suspender intervention, it is highly desirable of a scenario where the droplet can have a shape the same as that of a free-flying droplet, with minimized droplet-substrate contact area, and remain fixed in position during the entire drying process. Although there have been some experimental and numerical simulation studies on the interventions of suspenders on droplet evaporation rate, no study exists that caters to details on how the knob and plate suspenders lead to the occurrence of droplet climbing. Furthermore, concise and qualitative data to guide the design of suspender in SDD experiments are not available. It should be pointed out that the coating materials (hydrophobic or hydrophilic), size, and shape of the suspender can significantly contribute to the suspension state of the droplet.

In this study, a volume of fluid (VOF) model and droplet hanging state quantification methods were developed to simulate and analyze the process of hanging a droplet using different suspenders. This model allowed us to investigate the influences of the shape, size, and surface finishing materials of the suspender on the hanging behavior of droplets with variable properties. In addition, by scaling down the geometry, simulations were extended to hanging tiny droplets of 100 μm. The quantitative results will guide the rational design of suspenders that can offer minimized intervention with the lowest substrate-droplet contact area and the least droplet shape deformation.

2. Modeling and simulation methods

2.1. Geometric models

Two types of suspender models have been constructed, i.e., the plate model and the knob model. Fig. 1(a) shows the complete simulation domain for the plate model. A droplet attached to the plate suspender has been enlarged to show the detailed geometry. Boundary conditions used in the model are indicated in Fig. 1(b). Note that a 2D axisymmetric model was constructed. After computing the solution to the 2D axisymmetric problem, the 2D data can be revolved to generate 3D plots.

Table 3
Droplet properties and initial conditions.

Parameters		Notation	Model values	References
Temperature		T	298 K	
Water	Density	ρ_w	997.04 kg/m^3	(Ghauri and Ansari, 2006)
	Viscosity	μ_w	0.8904 × 10^{-3} Pa·s	(Ghauri and Ansari, 2006)
	Surface tension coefficient	σ_w	71.99 mN/m	(Vargaftik et al., 1983)
Skim milk	Density	ρ_m	1021 kg/m^3	(Solanki and Rizvi, 2001)
	Viscosity	μ_m	1.534 × 10^{-3} Pa·s	(Solanki and Rizvi, 2001)
	Surface tension coefficient	σ_m	47.29 mN/m	(Kristensen et al., 1997)
Ethanol	Density	ρ_e	785.8 kg/m^3	(Khattab et al., 2012)
	Viscosity	μ_e	1.099 × 10^{-3} Pa·s	(Khattab et al., 2012)
	Surface tension coefficient	σ_e	22.07 mN/m	(Sobac and Brutin, 2011)
Air	Density	ρ_g	1.225 kg/m^3	
	Viscosity	μ_g	1.789 × 10^{-5} Pa·s	
Gravitational acceleration		g	9.81 m/s^2	
Droplet in scale-normal model	Volume	V_1	1 mm^3	
	Diameter	D_1	1.24 mm	
Droplet in scale-down model	Volume	V_2	5.2 × 10^{-4} mm^3	
	Diameter	D_2	0.10 mm	

Finer mesh cells were utilized in the region closer to the suspender in order to capture the larger gradients (see Fig. 1(c)). The geometry, boundary conditions and the mesh for the knob model are given in Fig. 1 (d).

As introduced earlier, two types of models at different scales were investigated. The first model is called scale-normal model, which refers to the current experimental SDD system. The second one is called scale-down model, which is obtained by scaling down the geometry of the scale-normal model. It refers to a virtual system with much smaller suspenders and droplets, which is experimentally unavailable due to limitations of current experimental techniques. The values of the geometric parameter settings for the scale-normal and scale-down models are listed in Table 2.

2.2. Governing equations

The hanging process of a liquid droplet is a typical two-phase flow. The volume of fluid (VOF) method can characterize the flow of two or more immiscible fluids by solving a set of momentum equations and tracking the volume fraction of each fluid over the entire simulation region. Air is defined as the primary phase with volume fraction α_g, and the liquid droplet is the second phase with volume fraction α_l. Phase interface tracking for a two-phase system is accomplished by solving the continuity equation for the volume fraction of one phase. For the liquid phase, the volume fraction equation has the following form:

$$\frac{\partial \alpha_l}{\partial t} + \nabla \bullet (\alpha_l \boldsymbol{u}) = 0 \tag{1}$$

where α_l is the volume fraction of liquid phase; $\boldsymbol{u}$ is the velocity vector of liquid phase (m/s).

The volume fraction of the gas phase for a gas–liquid two phase system does not need to be solved since the addition of the volume fractions of the gas phase and the liquid phase is 1.

The continuity equation for the incompressible fluid and the following momentum conservation equation are solved over the computational domain and the velocity field obtained from the solution is shared between the phases:

$$\frac{\partial}{\partial t}(\rho \boldsymbol{u}) + \nabla \bullet (\rho \boldsymbol{u}\boldsymbol{u}) = -\nabla p + \nabla \bullet \left[\mu\left(\nabla \boldsymbol{u} + \nabla \boldsymbol{u}^T\right)\right] + \rho \boldsymbol{g} + F_{vol} \tag{2}$$

where p is pressure (Pa); g is gravitational acceleration (m/s^2). In a two-phase system, if the volume fraction of the second phase, i.e., the liquid phase, is tracked, the density ρ and viscosity μ in each control volume are:

$$\rho = \alpha_l \rho_l + (1 - \alpha_l)\rho_g \tag{3}$$

$$\mu = \alpha_l \mu_l + (1 - \alpha_l)\mu_g \tag{4}$$

where ρ_g, ρ_l are the densities of the gas and liquid phases, respectively (kg/m^3); μ_g, μ_l are the viscosities of the gas and liquid phases, respectively (Pa·s).

F_{vol} is the volumetric force due to surface tension. According to the continuum surface force (CSF) model proposed by Brackbill et al. (1992), surface tension can be interpreted as a continuous, three-dimensional effect across an interface. Surface tension effects are modeled by adding a source term in the momentum conservation equation.

$$F_{vol} = \sigma \frac{\alpha_l \rho_l \kappa_g \nabla \alpha_g + \alpha_g \rho_g \kappa_l \nabla \alpha_l}{\frac{1}{2}\left(\rho_g + \rho_l\right)} \tag{5}$$

where σ is the surface tension coefficient (mN/m). The model involves the gas and liquid phases only, then $\kappa_g = -\kappa_l$ and $\nabla \alpha_g = -\nabla \alpha_l$, and Equation (5) can be simplified as:

$$F_{vol} = \sigma \frac{\rho \kappa_l \nabla \alpha_l}{\frac{1}{2}\left(\rho_g + \rho_l\right)} \tag{6}$$

where ρ is the volume average density calculated by Equation (3). The interface curvature, κ_l, is defined in terms of the divergence of the unit normal, $\hat{n}$:

$$\kappa_l = \nabla \bullet \hat{n} \tag{7}$$

$$\hat{n} = \frac{\nabla \alpha_l}{|\nabla \alpha_l|} \tag{8}$$

where $\hat{n}$ is affected by the liquid contact angle θ on the suspender wall. The surface normal to the cell near the wall is:

$$\hat{n} = \hat{n}_s \cos\theta + \hat{t}_s \sin\theta \tag{9}$$

where θ is the equilibrium contact angle at the smooth wall, $\hat{n}_s$ and $\hat{t}_s$ are the unit vectors normal and tangential to the wall, respectively.

2.3. Initial and boundary conditions

The boundary conditions and mesh for the plate model are plotted respectively in Fig. 1(b) and Fig. 1(c). The bottom boundary of the computational domain is the air velocity inlet, with a value of 0 m/s, the top boundary is the pressure outlet, the boundary on the right side is set to symmetry, and the no-slip boundary condition is used for the suspender wall. Different contact angle values are set on the suspender wall to represent different surface finishing materials on the wall. To track the gas–liquid and liquid–solid interfaces more accurately, extremely fine meshes were generated in the area near the wall to capture the change of droplet shape and ensure the accuracy of the calculations. In this study, the diameter of the scale-normal water droplet used in the simulation is 1.24 mm (i.e., a 1 μL droplet), whereas a 100 μm diameter droplet size was used in the scale-down model. Initially, the droplet was

Table 4
Settings for the parametric study.

Model		Parameters	Value of Cases Setting	Notes
Scale-normal model	Knob	θ (°)	20, 24, 40, 60, 80, 90, 116.5, 120, 140	σ = 71.99 mN/m
	Plate	θ (°)	20, 24, 40, 60, 80, 90, 116.5, 120, 140, 160, 165	σ = 71.99 mN/m χ_n = 0.24
	Plate	σ (mN/m)	22.07	θ = 20°, 40°, 60°, 80°, 100°, 120°, 140° χ_n = 0.24
			47.29	θ = 20°, 40°, 60°, 80°, 100°, 120°, 140°, 155° χ_n = 0.24
			71.99	θ = 20°, 40°, 60°, 80°, 100°, 120°, 140°, 160°, 165° χ_n = 0.24
	Plate	χ_n	0.08	θ = 20°, 40°, 60°, 80°, 100°, 120° σ = 71.99 mN/m
			0.16	θ = 20°, 40°, 60°, 80°, 100°, 120°, 140°, 160° σ = 71.99 mN/m
			0.24	θ = 20°, 40°, 60°, 80°, 100°, 120°, 140°, 160°, 165° σ = 71.99 mN/m
			0.48	θ = 20°, 40°, 60°, 80°, 100°, 120°, 140°, 160°, 165°, 170° σ = 71.99 mN/m
			1.21	θ = 20°, 40°, 60°, 80°, 100°, 120°, 140°, 160°, 165°, 170° σ = 71.99 mN/m
Scale-down model	Plate	χ_d	0.08	θ = 20°, 40°, 60°, 80°, 100°, 120° σ = 71.99 mN/m
			0.16	θ = 20°, 40°, 60°, 80°, 100°, 120°, 140°, 160° σ = 71.99 mN/m
			0.24	θ = 20°, 40°, 60°, 80°, 100°, 120°, 140°, 160°, 165° σ = 71.99 mN/m
			0.48	θ = 20°, 40°, 60°, 80°, 100°, 120°, 140°, 160°, 165°, 170° σ = 71.99 mN/m
			1.21	θ = 20°, 40°, 60°, 80°, 100°, 120°, 140°, 160°, 165°, 170° σ = 71.99 mN/m

patched into the simulation domain with a very small contact area between the droplet and the bottom surface of the suspender (Fig. 1(a)). Water, skim milk, and ethanol were selected as representative droplets, whose properties are listed in Table 3. Water, skim milk and ethanol droplets were chosen for the following reasons: water is used as a solvent in many of the experimental droplets of SDD, and ethanol (a representative organic solvent), is also chosen as a solvent for the experimental droplets of SDD (Fu et al., 2011; Su et al., 2020). SDD is also commonly used to achieve realistic detection of the drying behavior of single milk droplets during convective air drying (Lin and Chen, 2002).

2.4. Hanging state analysis

The contact area ratio, δ, is the ratio of the liquid–solid contact area to the overall surface area of the droplet, which is the sum of the liquid–solid contact area and the liquid–gas contact area. A smaller value of this ratio indicates a less intrusive suspender. It is defined as:

$$\delta = S_{sl} / \left(S_{sl} + S_{lg}\right) \tag{10}$$

where S_{sl} is the area of the contact surface between the wall of the suspender and the droplet (m^2); S_{lg} is the area of the contact surface between the liquid and gas (m^2).

The droplet oscillates on the suspender before reaching the steady state. The average amplitude ratio (Tan et al., 2019), $\overline{\beta}$, is used to characterize the significance of the oscillation process:

$$\begin{cases} \beta_n = \max(A_n, A_{n+1}) / \min(A_n, A_{n+1}) \\ \overline{\beta} = \dfrac{1}{n-1} \sum_1^n \beta_n \end{cases} \tag{11}$$

where β_n is the ratio of the large amplitude to the small amplitude of two adjacent cycles, i.e., $\max(A_n, A_{n+1})/\min(A_n, A_{n+1})$.

When the oscillation amplitude ratio of the droplet, β_n, is less than 1.001, the droplet is considered to have reached the steady state. The droplet oscillation duration, ε, is used to represent the time for the droplet to reach the steady state (ms).

Droplet sphericity quantifies the extent of droplet deformation from a sphere. The closer the value is to 1, the closer the droplet is to a sphere:

$$\Psi = \frac{S_e}{S_{sl} + S_{lg}} \tag{12}$$

where S_e is the surface area of the volume equivalent sphere (mm^2).

The suspended droplets reach force equilibrium under the competition of gravity and surface tension. The Bond number is the ratio of droplet gravity to surface tension, implying relative importance of two forces (Bond, 1935):

$$Bo = \frac{\Delta \rho g D^2}{4\sigma} \tag{13}$$

where $\Delta\rho$ is the difference in density between the droplet and the air (kg/m^3); g is gravitational acceleration (m/s^2); D is the diameter of the droplet (mm).

2.5. Computational settings

In this study, the conservation equations were solved using the Pressure-Based Solver in FLUENT 18.1, a commercial CFD software based on the finite volume method. In the solution derivation process, the primary phase is air and the secondary phase is liquid water. For the spatial discretization scheme, Least Squares Cell Based scheme was used for the gradient format. The PRESTO (Pressure Staggering Option) scheme was used in pressure interpolation and the Second Order Upwind was used to solve the momentum equation. The volume fraction discretization scheme for transient flows in VOF simulations is the Geo-Reconstruct format, which allows accurate tracking of the free surface. For pressure, density, body forces, and momentum; the under-relaxation factors are 0.3, 1, 1, and 0.7, respectively. The time step for the scale-normal model is 5×10^{-7} s, and for the scale-down model is 5×10^{-8} s. For comparison and discussions, the settings for all cases are listed in Table 4.

2.6. Mesh independence study

Mesh independence was verified for the normal-scale knob suspender and plate suspender models, with each model geometry divided

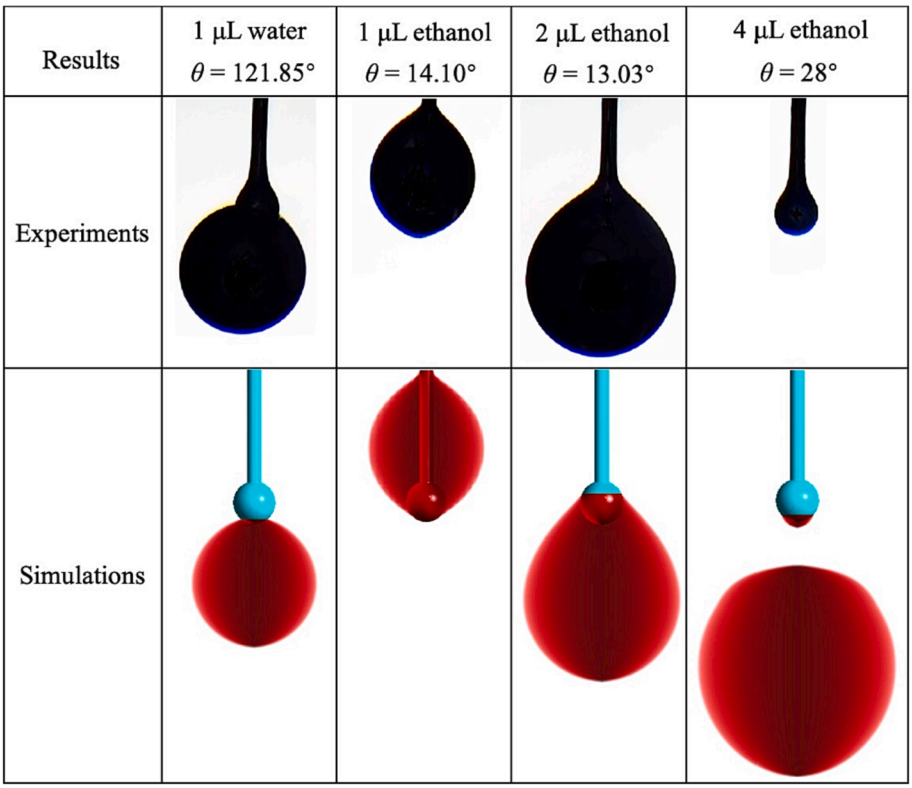

Fig. 2. Comparison between experimental and simulation results for water and ethanol droplets hanging on a 422 μm diameter PTFE-coated knob suspender. The contact angles for 1 μL water droplet, 1 μL, 2 μL, and 4 μL ethanol droplets on a PTFE-coated slide surface were measured to be 121.85°, 14.10°, 13.03°, and 28°, respectively. The 4 μL ethanol droplet fell off from the knob suspender in the experiment, whose result shows a knob only.

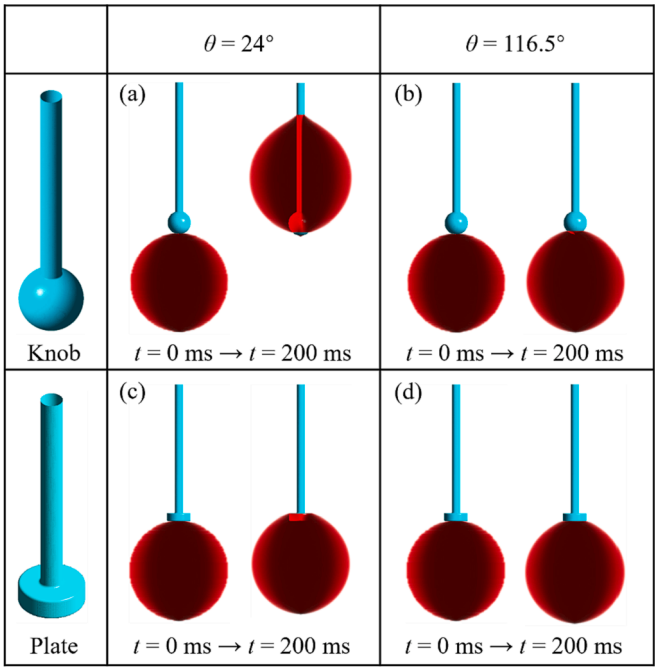

Fig. 3. Suspension state of droplets at different contact angles ($\theta = 24°$ and $\theta = 116.5°$) in two scale-normal models: (a) and (b) knob model; (c) and (d) plate model. Both initial state ($t = 0$ ms) and final state ($t = 200$ ms) of the droplet for four cases are plotted for comparison.

into four meshes of different densities. The total number of mesh cells are 70,921 (mesh 1), 82,257 (mesh 2), 94,301 (mesh 3) and 117,609 (mesh 4) for the knob suspender, and are 75,039 (mesh 1), 84,828 (mesh 2), 98,330 (mesh 3) and 118,500 (mesh 4) for the plate suspender respectively. For the two types of suspender models, there is no significant difference in the contact area ratios calculated using different density meshes after the droplet finally reaches the steady state. In order to ensure the accuracy of the calculations, capture the interfacial changes accurately, and save the computational cost, the mesh 3 configuration (i.e., the mesh in Fig. 1) was chosen in this study.

3. Results and discussion

3.1. Model validation

Fig. 2 shows the comparison between experimental and simulation results for different-sized water and ethanol droplets suspended on a 422 μm polytetrafluoroethylene (PTFE)-coated knob suspender. The simulation results match experimental data quite well not only in terms of the hanging state but also the shape of the droplets. Both experiment and simulation show that a PTFE-coated knob suspender with a contact angle of 121.85° can hold a 1 μL water droplet. In experiments for ethanol droplets, the 1 μL ethanol droplet completely wetted the knob and climbed up along the rod. The 2 μL ethanol droplet wetted most part of the knob only. The 4 μL ethanol droplet, however, fell off from the suspender. Our simulations successfully captured this trend. Since the surface tension of water is more than three times larger than that of ethanol, the sphericity of water droplet is higher than that of the ethanol droplets, which has been confirmed by both simulation and experimental results.

There are several possible reasons for the deviation of the droplet from the centreline of the suspender in the experiments. The knob suspender was made by hand, so it is difficult to obtain a perfectly spherical shape, and imperfections in the shape of the suspender may drive the droplet to deviate from the centreline. Also, PTFE was manually sprayed on the surface of the knob suspender, and it is almost impossible to

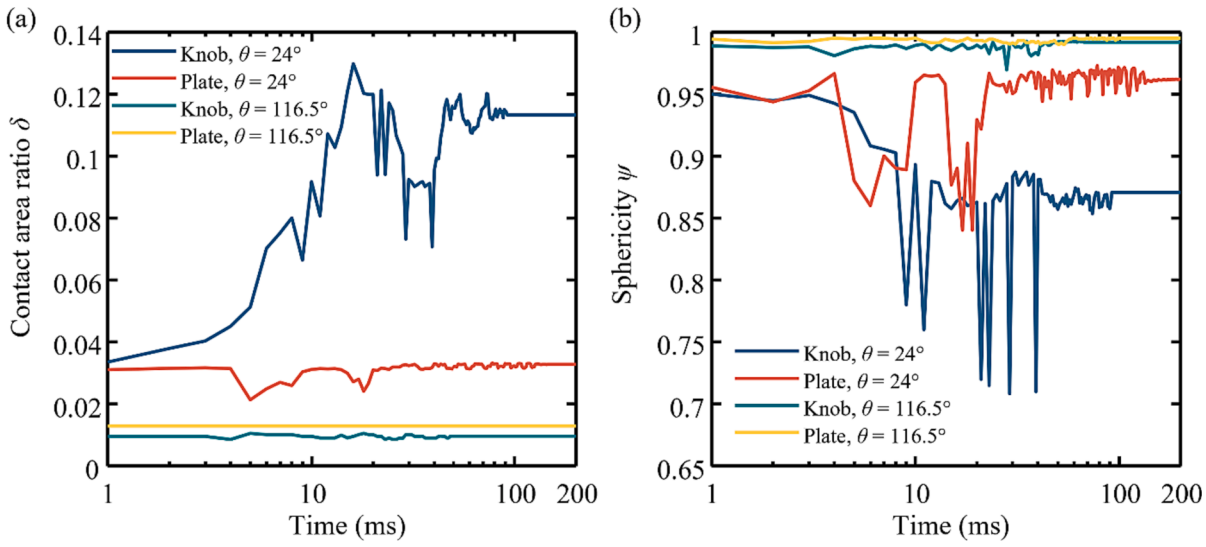

Fig. 4. Droplet oscillation for the knob model and the plate model: (a) contact area ratio as a function of time; (b) droplet sphericity as a function of time.

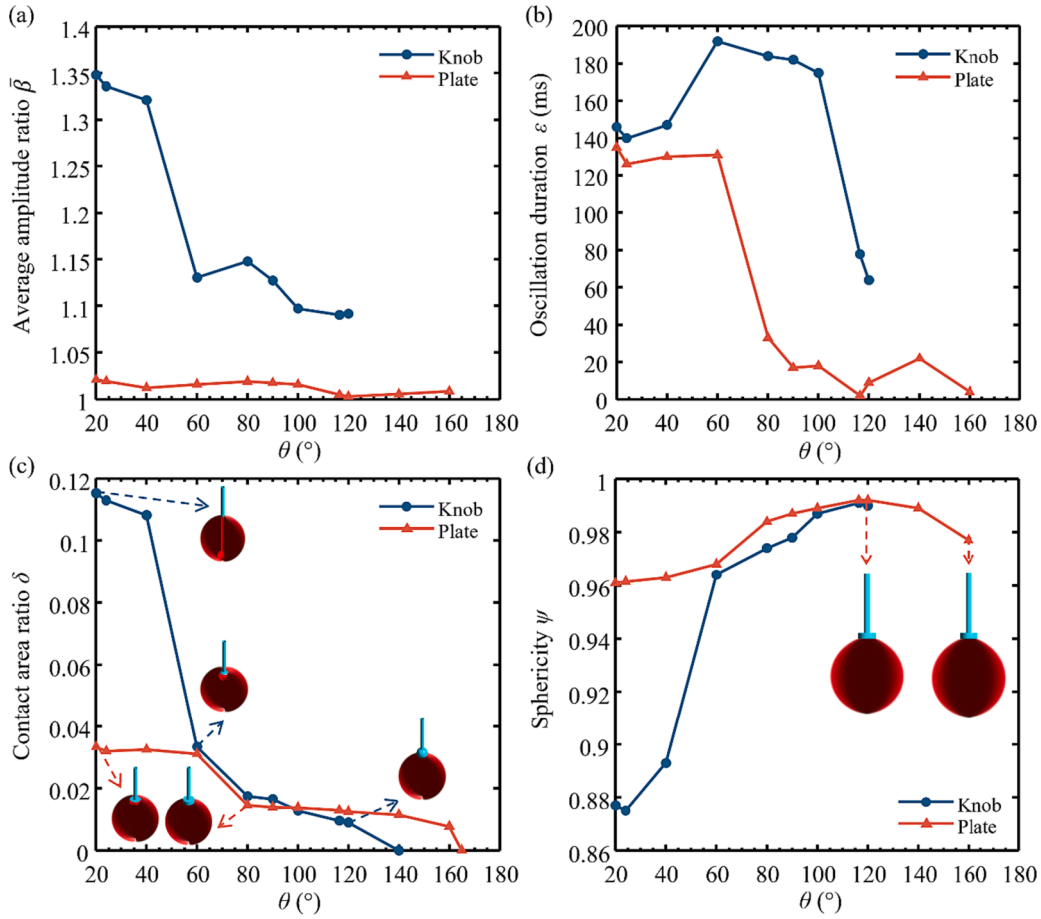

Fig. 5. Comparison of knob model and plate model in the contact angle range from 20° to 180°: (a) average amplitude ratio; (b) oscillation duration; (c) contact area ratio; (d) sphericity.

ensure a uniformly distributed coating at this stage. Moreover, a slim glass filament was used to transfer a droplet to the suspender, followed by the retrieval of the filament from one side (i.e., the left side in this work). This retrieval operation could lead to the shift of droplet position from the centreline. Also note that due to the restriction of our current experimental technique, at this stage, we cannot prepare a smooth surface with a contact angle much higher than 120°. Replacing smooth surfaces by 3D-printed structured surfaces may be an option, but it is out of the scope of this work.

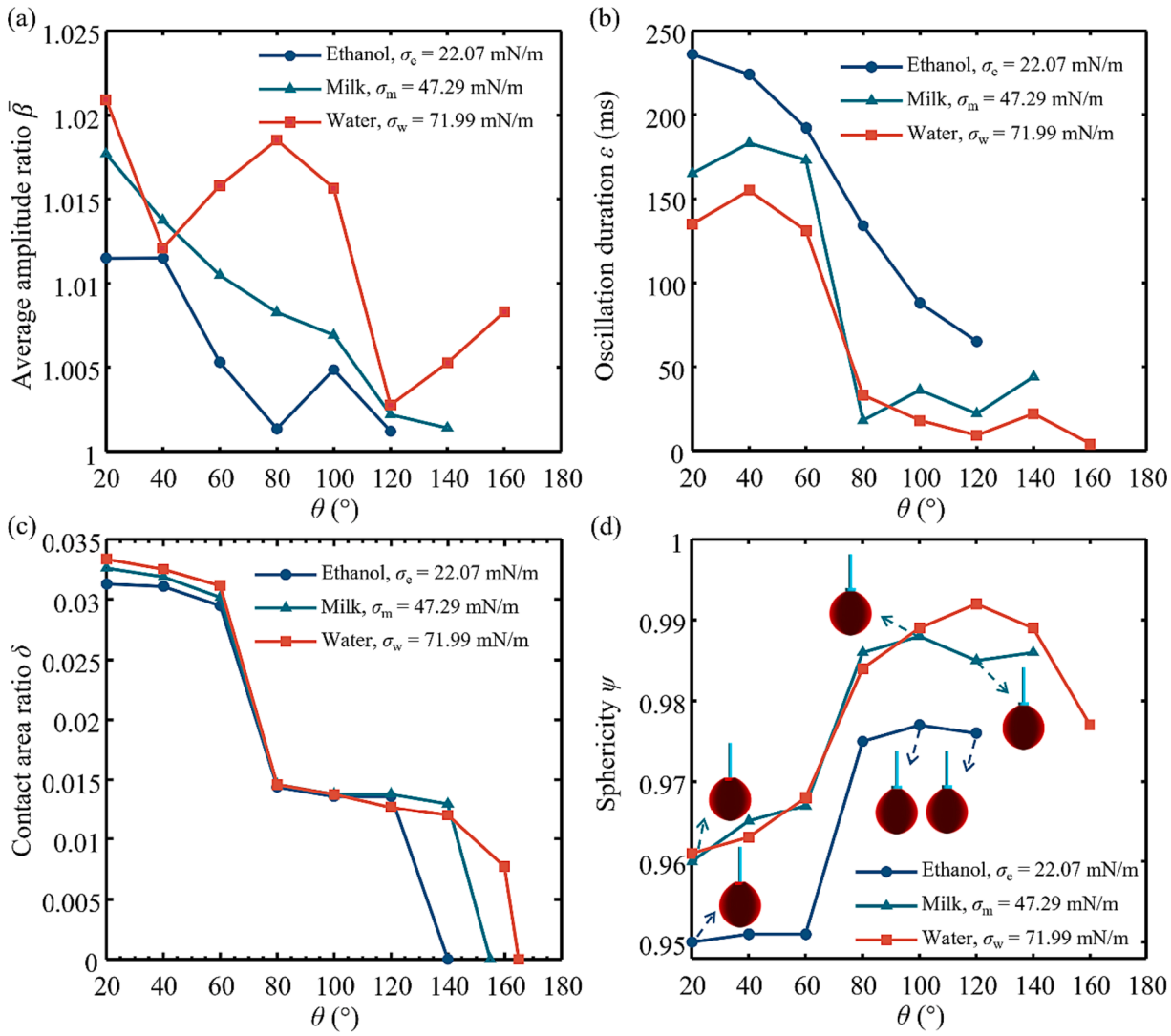

Fig. 6. Droplets of different surface tension hung on a plate suspender in the contact angle range of 20° to 180°: (a) average amplitude ratio; (b) oscillation duration; (c) contact area ratio; (d) sphericity.

3.2. Effect of the shape of the suspender on droplet hanging state

The effects of two different suspender shapes and contact angles on the suspension state of water droplets were investigated. Traditional spherical knob suspender and newly-developed plate suspender are plotted in Fig. 3. The contact angles were set to 24° (Tong et al., 2015) and 116.5° (Paria et al., 2015), which are the contact angles of water droplets on smooth glass and polytetrafluoroethylene (PTFE) or Teflon coated surfaces at room temperature respectively.

At a contact angle of 24°, the droplet on the knob suspender climbed up along the rod (Fig. 3(a)), while the droplet on the plate suspender only climbed the side wall of the suspender (Fig. 3(c)). Although both surfaces are hydrophilic (Fig. 3(a) and Fig. 3(c)), the plate suspender effectively prevents the droplet from climbing the rod. At a contact angle of 116.5°, no climbing of the droplets on the knob suspender occurred (Fig. 3(b)), and the droplet on the plate suspender hung on the lower wall of the suspender (Fig. 3(d)).

As shown in Fig. 4, for both plate and knob systems, the droplet experiences the oscillation process before reaching the steady state. The oscillation amplitude as well as the oscillation duration of the droplet for the contact angle of 24° are larger than those for the contact angle of 116.5°. After the droplet reaches steady state with contact angle of 24° for the plate model and the knob model, the contact area ratio is larger than that for the contact angle of 116.5°. Also, the droplet sphericity is less for a contact angle of 24° than that for 116.5°.

At a contact angle of 24°, droplet climbing takes place for the knob model only (see Fig. 3(a)). Thus, the contact area ratio of the knob model is much larger than that of the plate model, and the droplet sphericity is much smaller than that of the plate model. When the contact angle is 116.5°, the contact area ratio of the plate model is slightly larger than that of the knob model, and the droplet sphericity of the knob model is slightly smaller than that of the plate model. The comparisons tell us, at a hydrophilic contact angle of 24°, the plate model can effectively prevents droplet from climbing on the rod. At a hydrophobic contact angle of 116.5°, the contact area ratios of the plate model and knob model are nearly the same and are both smaller, implying less heat transfer from the suspender for single droplet drying. They also have relatively similar droplet sphericity with larger values, that is, the droplets are close to a sphere in shape.

Can the increase of the contact angle beyond 116.5° further reduce the intervetion of the suspender? Will the decrease of the contact angle below 24° lead to the droplet climbing for the plate model? To answer these questions, the effects of the contact angle in the range of 20° to 180° on the suspension state of droplets for both plate and knob models were investigated. After the droplet was hung on the suspender, it underwent a process of oscillation and then reached the steady state. The

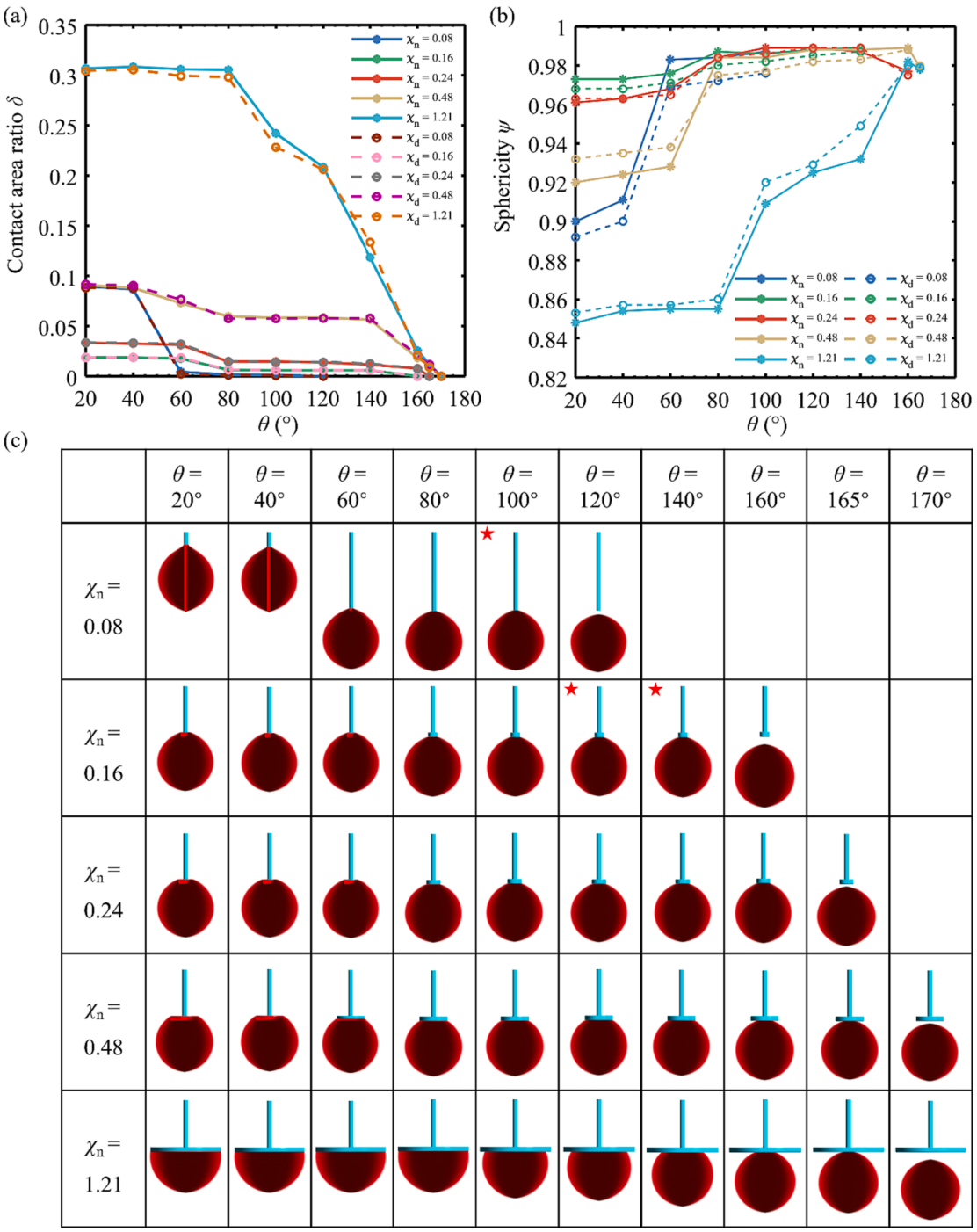

Fig. 7. Comparison of different radius plate models in the contact angle range of 20° to 180°: (a) comparison of contact area ratio of scale-normal model (solid line) and scale-down model (dotted line); (b) comparison of sphericity of scale-normal model (solid line) and scale-down model (dotted line); (c) Suspension state diagram of droplets for the scale-normal model (red stars are the optimum results).

average oscillation amplitude and oscillation duration of the droplets hung on the plate model and knob model tend to decrease with the increase of contact angle (Fig. 5(a) and (b)). At the same contact angle, the average amplitude ratio and oscillation duration of the droplets hung on the plate model are smaller than those of the knob model. Compared with the knob model, the droplet hanging on the plate model has much less oscillation amplitude during the hanging process, and the droplet is more stable and able to reach the steady state in a shorter time. As shown in Fig. 5(c), for both models, the contact area ratio decreases with increasing contact angle, signifying that the heat transfer from the suspender decreases with increasing contact angle and the intrusive effect of the suspender decreases. A smaller contact angle means that the suspender has a better wetting behavior, which can enhance the heat transfer between the suspender and the droplet (Zhang et al., 2016). When the contact angle is less than 60°, the contact area ratio of the knob model is considerably larger than that of the plate model because the droplet hanging on the knob model is climbing the rod, while the droplet hanging on the plate model is not. The difference in contact area ratio between the knob model and the plate model is very small for contact angles in the range of 60° and 120°. Within this contact angle range, when droplets are hung on the two models, the effect of the suspender on the intrusiveness of the droplets is almost identical. As the

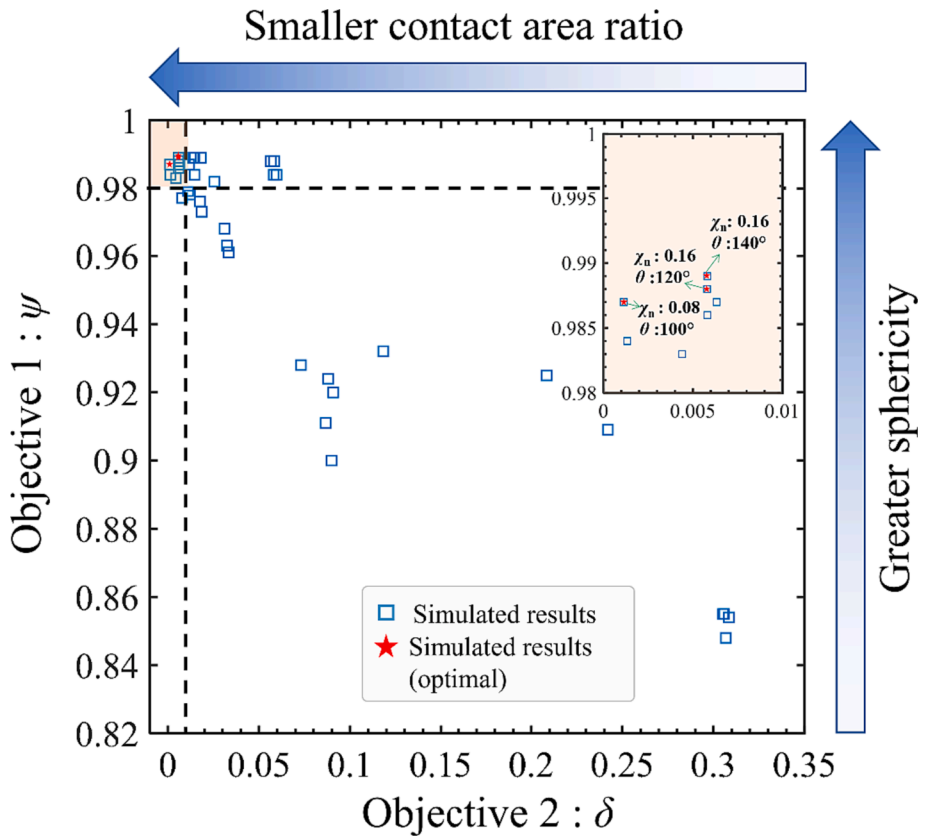

Fig. 8. Design scheme of the plate models. The data points in the graph are the values of the two objectives (contact area ratio and sphericity) corresponding to χ_n and contact angle in all cases. The shaded area shows the range containing optimized design options.

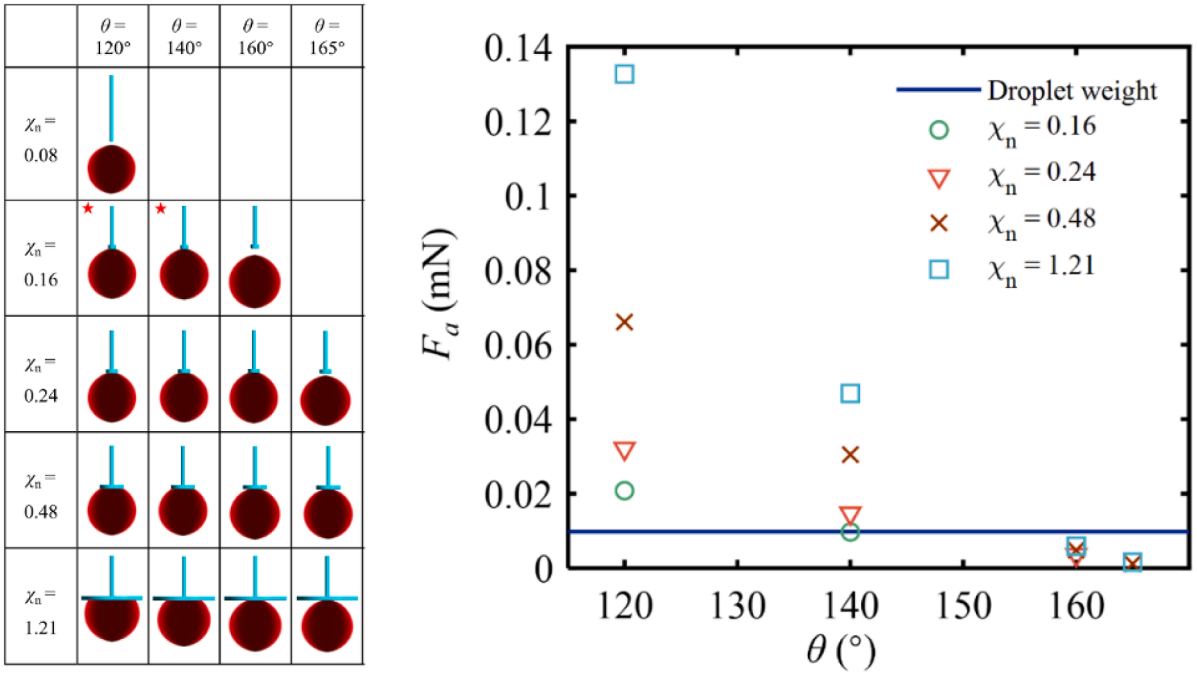

Fig. A1. The comparison between the pull off force needed to separate the droplet from the suspender and the weight of the 1 μL droplet. The predicted hanging states of droplets at different conditions are given on the left side, which is part of Fig. 7.

contact angle was increased to 140°, the droplets hung on the knob model fell off, whereas the droplets hung on the plate model fell off only when contact angle was increased to 165°. Droplets hung on the plate model have larger sphericity than those hung on the knob model over the whole range of contact angles as shown in Fig. 5(d). For the latter, the sphericity increases with the increase of contact angle (Huang et al.,

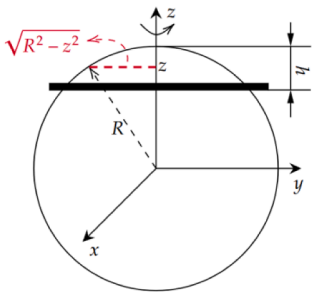

Fig. A2. Schematic diagram for the calculation of the droplet volume.

2012). In contrast, the sphericity of the droplets hung on the plate model increases then decreases with the increase of contact angle. Similar to the contact area ratio, the droplet sphericity of the two models is nearly comparable for the same contact angle in the range of 60° to 120°. For the plate model, the sphericity of the droplet decreases with the increase of the contact angle greater than 120°. This is because as the contact angle increases, the decrease in contact area between the droplet and the suspender is smaller than the increase in contact area between the droplet and the gas. The droplet deforms more obviously under the influence of gravity. Compared with the knob suspender, the plate suspender can effectively prevent droplets from climbing rod under hydrophilic contact angle, and has a larger contact angle fitness range (i.e., 20° to 165°). In the range of 80°-140°, the contact area ratio is lower than 0.02 and the sphericity is higher than 0.98, i.e. the intrusive influence of the suspender is insignificant. For single droplet drying equipment, the plate model is more suitable for hanging droplets.

3.3. *Effect of droplet surface tension on droplet hanging state*

Among common liquids, the surface tension of water is relatively large, i.e., 71.99 mN/m at room temperature. Skimmed milk droplets and ethanol droplets have lower surface tension values than water, which are 47.29 mN/m and 22.07 mN/m, respectively. They were

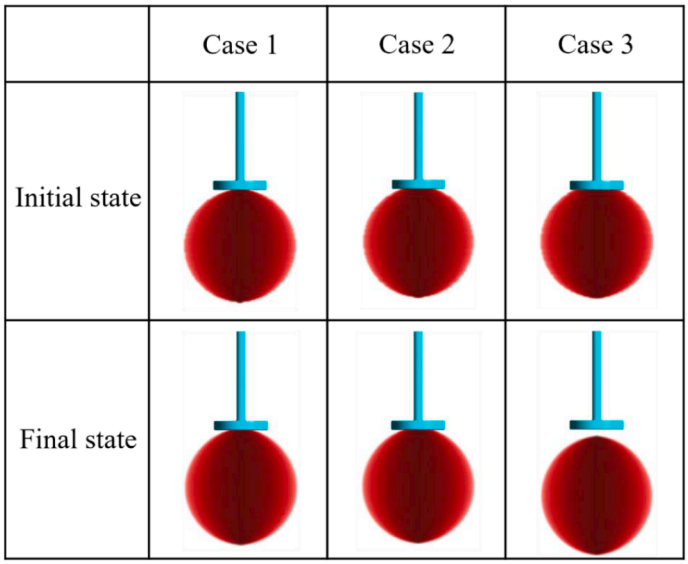

Fig. A3. Comparison of droplets' final hanging states under three different initial states. Although the suspender in Cases 1 and 2 can hold the droplet, Case 3 cannot.

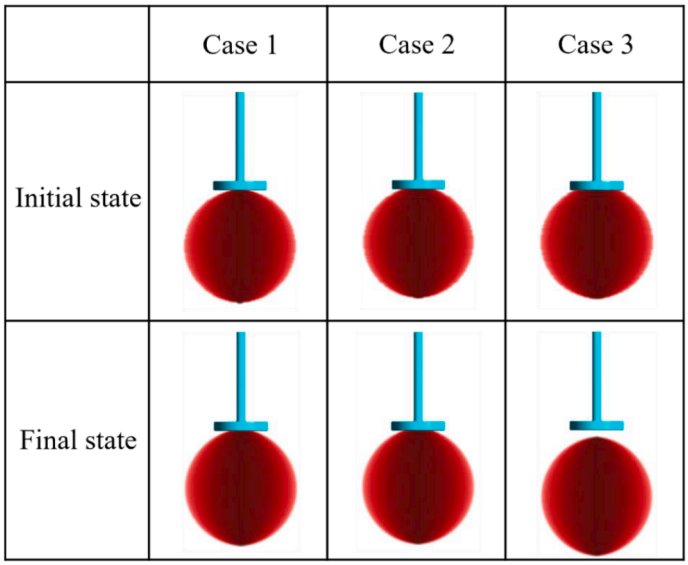

Fig. A4. Droplet oscillations before reaching the steady state under three different initial states: (a) contact area ratio as a function of time; (b) droplet sphericity as a function of time. The droplet in Case 3 fell off from the suspender (at ~10 ms) during the oscillation process.

selected to investigate the effect of surface tension on the hanging state of droplets on a plate suspender. The Bond numbers (Bo) for 1 μL water, skim milk, and ethanol droplets are respectively, 0.052, 0.082, and 0.134. The smaller the Bond number, the greater the effect of surface tension on the droplet, and the smaller the effect of gravity (Dang et al., 2022). The average oscillation amplitude and oscillation duration of the three droplets tend to decrease with the increase of contact angle. Also, the larger the surface tension of the droplet, the larger the average oscillation amplitude and the smaller the oscillation duration and vice-versa (see Fig. 6(a)). The surface tension of water is much higher than that of ethanol, and its average oscillation amplitude is significantly higher than that of ethanol droplets. On the other hand, its oscillation duration is smaller than that of ethanol droplets (Fig. 6(b)).

In the contact angle range of 20°-60°, ethanol, milk, and water droplets all climbed the side walls of the plate, and the droplets with higher surface tension had a slightly higher contact area ratio than the droplets with smaller surface tension at the same contact angle (Fig. 6 (c)). The sphericity of ethanol droplets was significantly smaller than that of milk and water droplets (Fig. 6(d)). Due to the smaller surface tension of ethanol, its droplet shape appeared elongated and elliptical compared to the other two droplets. As the contact angle increases to 80° and greater (but smaller than 120°), all three droplets hung on the bottom-wall surface of the plate. Their contact area ratios are almost the same when the contact angles are the same. Although the sphericity of ethanol droplets is significantly smaller than that of milk and water droplets, ethanol droplets have ellipsoidal shape instead of spherical shape compared to milk and water droplets due to their smaller surface tension. Surface tension tends to keep the droplet in a spherical shape, while gravity tends to elongate the droplet. The greater the surface tension of a droplet, the closer the droplet's shape is to a spherical shape (Saad and Neumann, 2016).

As the contact angle increased further beyond 120°, the ethanol droplet with the minimum surface tension was the first to fall from the pendant at a contact angle of 140°. This is followed by the skim milk droplet with a higher surface tension falling at 155°. The water droplet with the maximum surface tension fell at 165°. The Bo numbers of three droplets are different and are influenced by gravity and surface tension to different degrees. Ethanol has the largest Bo and is more affected by gravity than the other two droplets, so it fell from the plate at a much smaller contact angle of 140°. For droplets with different surface tensions, the difference in contact area ratio is small when the contact angles are the same. But the threshold fall-off contact angle increases with increase in surface tension. The droplet's sphericity is also influenced by its surface tension of droplets, that is, the higher the surface tension, the greater the sphericity of a droplet. For a droplet with a given surface tension, a plate suspender with a contact angle in the range of 80° to 120° should be selected, in which case a small contact area ratio and a large droplet sphericity can be ensured.

3.4. Effect of suspender size of plate model on droplet hanging state

A parametric study of the influence of plate size as well as contact angle on the droplet suspension state was conducted. The droplets were chosen as the representative water. Five different plate sizes were investigated with $\chi_n = 0.08$, 0.16, 0.24, 0.48, and 1.21, where χ_n is the ratio of $2R_{n\text{-}p}$ to D_1. D_1 is the diameter of a 1 μL droplet, which is 1.24 mm, and $2R_{n\text{-}p}$ is the diameter of the plate in the Scale-normal model. $\chi_n = 0.08$ is the case where the suspender and the rod have the same radius. $\chi_n = 0.24$ is the case studied in previous two sections. In the cases where χ_n is 0.08, 0.16, 0.24, and 0.48, the average amplitude ratio and the oscillation duration of the droplet both tend to decrease with the increase of the contact angle. As shown in Fig. 7(a), for different values of χ_n, the contact area ratio decreases as the contact angle increases. At the same contact angle, the contact area ratio increases with increasing χ_n. The larger the contact angle and the smaller the χ_n, the less the intrusiveness of the suspender. For the case of $\chi_n = 0.08$ and the contact angle between 20° and 40°, the droplet climbed the rod, resulting in the increased contact area ratio, and enhanced intrusive influence of the suspender (Fig. 7(c)). When the contact angle is between 60° and 100°, the droplet hung on the bottom wall of the plate. However, when the contact angle increased to 120°, the droplet fell off from the suspender. For χ_n of 0.16 and 0.24, the droplet climbed up the sidewall of the plate suspender for contact angles in the range of 20° and 60°, but did not continue to climb up the rod. As the contact angle continues to increase, the droplet hung on the bottom wall of the plate suspender. For χ_n of 0.16, 0.24, and 0.48, the contact angles of droplets falling from the suspender are 160°, 165°, and 170°, respectively. As χ_n increased to 1.21, the droplets did not climb to the side wall of the plate suspender even when the contact angle was lower than 40°. As the contact angle increases further, the contact area between the droplet and the wall surface decreases significantly (see the last row in Fig. 7(c)), and thus the contact area ratio decreases (the light blue line in Fig. 7(a)). When the contact angle increased to 170°, the droplets fell off from the suspender.

Fig. 7(b) demonstrates that the sphericity of the droplets tends to increase with increasing contact angle for different χ_n. When $\chi_n = 0.16$, 0.24, and 0.48, the sphericity is above 0.96 for the cases at a contact angle from 80° to 120°. The corresponding data points of contact area ratio δ and sphericity ψ for different χ_n and contact angles are plotted in Fig. 8.

After specifying the threshold values for the two objectives (0.01 for the contact area ratio and 0.98 for the sphericity), the range containing optimized design options can be identified (see Fig. 8). The closer to the top left choice in Fig. 8, the smaller the contact area ratio and the larger the droplet sphericity. Following the principle of selecting the best among the best, the three optimal designs can be identified from Fig. 8 (red stars in the figure). The corresponding suspension state diagrams of the droplets are shown in Fig. 7(c) with red stars as indicators. By controlling the χ_n and contact angle, a smaller contact area ratio with a larger sphericity can be obtained, providing guidance for the design of an ideal plate suspender.

3.5. Discussion on the feasibility of using superhydrophobic surfaces

Although CFD simulations predicted that suspenders with surfaces having a contact angle up to 165° could suspend a droplet (see results in Fig. 7), it will be extremely difficult to reproduce the hanging state using superhydrophobic surfaces in practice. Thus, under practical circumstances, superhydrophobic surfaces should be avoided in suspender design.

Note that simulation results for superhydrophobic surfaces in Fig. 7 were obtained under ideal conditions. In our model, the following assumptions were made: (1) the surface is ideally smooth with a roughness of zero, (2) superhydrophobic coatings are uniformly applied to the surface, and (3) the system is axially symmetric. These ideal conditions could be hardly achieved in real experiments. Moreover, for highly non-wettable surfaces, the adhesion force between the droplet and the superhydrophobic surface can hardly support the weight of the droplet (see calculations in Appendix I) and the final hanging state of droplets are sensitive to the initial state of the droplet (see simulations results in Appendix II). In real experiments, precise control of the initial shape of the droplet as close as possible to its steady-state shape is very challenging.

3.6. Discussion on the small-scale model predictions

The initial size of droplets used in glass filaments single droplet drying experiments is usually 0.5 mm-2 mm, which is more than ten times larger than the size of atomized droplets in an actual spray dryer as well as airborne droplets and aerosols. Since it is not feasible to scale down droplets in experiments, since it is difficult to replicate the tiny single droplet suspended on a very thin glass filament in actual situations. Notwithstanding, smaller droplets can be analyzed by numerical

simulations. A droplet diameter of 100 μm was chosen, which is the general size of a real atomized droplet in an industrial spray dryer (Lin and Chen, 2002). The scale-down model was obtained by scaling down the plate model in the above case by a factor of 12.4 (see Table 2 for the specific parameter settings of the base model). Fig. 7(a) compares the contact area ratios of the scale-normal model and the scale-down model. In the two scales, the contact area ratio is almost identical at the same contact angle for a certain ratio of plate radius to droplet radius, i.e., the same value of χ_d. Fig. 7(b) compares droplet sphericity under the scale-normal model and scale-down model, and the trend of droplet sphericity with contact angle is consistent for the two scales. The droplet sphericity differs between the two scales when χ and the contact angle are given. When the droplet size is 100 μm, the effect of gravity is significantly diminished. The effect of surface tension increases, so that the sphericity is different compared to the droplet at 1240 μm. The results tell us the suspender design solutions for normal-scale droplets are applicable to down-scale droplets.

4. Conclusion

In this work, the effect of suspender on droplet suspension state was investigated by multiphase flow CFD simulations. Through a series of numerical simulations, the intervention of various suspenders and their effects on droplet suspension state and droplet sphericity have been studied.

The cases of knob and plate suspenders, both with a diameter of 300 μm, were compared to reveal the effectiveness of the plate suspender in stopping the droplet climbing behavior. The effects of suspender shape, plate suspender size, and contact angle on the droplet hanging process were systematically explored. It was found that, regardless of the variation of suspender shape and plate suspender size, the suspender-droplet contact area ratio decreases with the increase of contact angle. For each type of suspender, the best contact angle value is available, which results in the lowest contact area ratio and the highest droplet sphericity. In addition, the suspension states of droplets with different surface tensions were explored. The variability of the effect of suspender on the intrusion of different droplets was small, but the difference of droplet surface tensions led to a large difference of droplet sphericity. Simulation results also show that the suspender design solutions obtained for the system hanging millimeter scale droplets can be applicable to the small-scale system hanging 100 μm droplets.

This work can be used to guide the design of a suspender for hanging a droplet with minimum intervention. The design is expected to reduce the invasiveness of the suspender and make the effect of the suspender on droplet drying kinetics negligible. For future work, it will be interesting and important (though challenging) to explore the underlying mechanism for the contact line pinning phenomenon observed for the plate suspender.

Declaration of Competing Interest

The authors declare that they have no known competing financial interests or personal relationships that could have appeared to influence the work reported in this paper.

Data availability

Data will be made available on request.

Acknowledgments

We are grateful for the financial support from the National Natural Science Foundation of China (21978184, 22178239), the “Jiangsu Innovation and Entrepreneurship (Shuang Chuang) Program”, the “Jiangsu Specially-Appointed Professors Program”, and the “Priority Academic Program Development (PAPD) of Jiangsu Higher Education Institutions”. We greatly appreciate critical, insightful and constructive comments from two anonymous reviewers.

Appendix I:. Theoretical calculation of adhesion force

For those simulation results in Fig. 7, theoretical analyses can be carried out to check the feasibility of hanging a 1 μL droplet on a hydrophobic surface with a contact angle between 120° to 160°. As suggested by Tadmor et al. (2017), we consider the system of a droplet on a flat surface for which the detachment starts from the solid–liquid interface. The pull off (adhesion) force needed to separate a liquid droplet from a flat solid surface can be calculated. The idea is that if the pull off force is higher than the weight of the droplet, that surface should be able to hold the suspended droplet. Derivation steps of the pull off force are given below.

The solid–liquid work of adhesion is given by the Dupré equation:

$$W_{sl} = \gamma_l + \gamma_s - \gamma_{sl} \tag{A1}$$

where W_{sl} is the liquid–solid work of adhesion per unit area (mJ/m^2); γ_{sl}, γ_l and γ_s are the solid–liquid, liquid–vapor and solid–vapor interfacial energies (mJ/m^2), respectively.

The Young-Laplace equation correlates the contact angle with interfacial energies:

$$\cos\theta = \frac{\gamma_s - \gamma_{sl}}{\gamma_l} \tag{A2}$$

where θ is the equilibrium contact angle at the smooth surface.

Combining and rearranging Eq's. (A1) and (A2) yields the Young-Dupré equation.

$$W_{sl} = (1 + \cos\theta)\gamma_l \tag{A3}$$

This equation relates the work of adhesion to the equilibrium contact angle. The work of adhesion per unit area (mJ/m^2) equals the pull off (separation) force per unit triple line circumference (Tadmor et al., 2017). The pull off force F_a can then be obtained by:

$$F_a = W_{sl} L_{TCL} = (1 + \cos\theta)\gamma_l L_{TCL} \tag{A4}$$

where L_{TCL} (mm) is the circumference of the triple-phase contact line. For the cases in Fig. 7, γ_l is the surface tension coefficient of water, i.e., σ_w. Eq. (A4) becomes:

$$F_a = (1+\cos\theta)\sigma_w L_{TCL} \quad (A5)$$

where θ is the equilibrium contact angle at the smooth surface, which is the contact angle specified in the model as a boundary condition at the suspender surface. L_{TCL} (mm) is the circumference of the triple-phase contact line, which can be read from the simulation results.

The comparison between the calculated pull off force F_a and the weight of a 1 μL droplet is given in Fig. A1. As shown in this figure, for most suspenders that we predicted through CFD simulations to be capable of holding a droplet, the pull off force needed to separate the droplet from the suspender is higher than the weight of the droplet. Theoretical calculation results confirm the feasibility of hanging a 1 μL droplet on a highly non-wettable surface (with a contact angle between 120 and 140°).

One may notice that there are exceptions in Fig. A1 for several cases of very high contact angles (160° and 165°), where the pull off force is slightly less than the droplet weight. One possible reason is that Eq. (A5) may underestimate the pull off force (Adam and Livingston, 1958). Furthermore, even if a smooth surface reaching a contact angle of 160° and above is available in the experiment, it will be very difficult to reproduce the hanging state for repeated experiments. It is because for such highly non-wettable surfaces, the hanging state of droplets are very sensitive to the initial state of the droplet, which can be justified by simulation results in Appendix II. In the experiment, precise control of the initial contact of the droplet and the suspender is very challenging.

Appendix I. I: Simulations for superhydrophobic surfaces under different droplet initial conditions

Take the case with contact angle of 165° and χ_n of 0.48 in Fig. 7 as an example, we prepared three initial states of the droplet and carried out in silico experiments. To make sure three cases have the same droplet volume of 1 μL, we first did geometric calculation. Fig. A2 shows a schematic diagram of the volume calculation for a droplet hanging under the plate suspender.

Removing the cap with the height of h, the remaining part of the sphere with the radius of R should be the volume of the droplet,

$$V = \frac{4}{3}\pi R^3 - \pi h^2 R + \frac{1}{3}\pi h^3$$

Given any cap height h, the sphere radius R can then be calculated to maintain the droplet volume to be 1 μL. For the simulation case in Fig. 7, h was set to be 0.005 mm. Two more cases with h of 0.030 mm and 0.055 mm were designed. Note that we integrated the volume of the droplet in the model and confirmed that three droplets have the same volume of 1 μL.

Fig. A3 shows comparisons of the initial and final droplet hanging states under three different initial droplet states. As h increases, the initial contact area between the droplet and the suspender increases. The droplet undergoes a series of shape deformations before reaching a steady state. When the difference between the initial state of the droplet and the steady state is greater, the droplet needs to undergo more vigorous and longer oscillation process (see Fig. A4), which may lead to the falling of droplet from the suspender. Droplet in the last case fell off from the plate suspender (see Fig. A3 and Fig. A4).

Simulation results suggest that highly non-wettable smooth surfaces with a contact angle of 160° and above are not recommended to hang droplets, since the adhesion force between the droplet and surface is very weak and the hanging state is very sensitive to the initial state of the droplet. Findings from our simulations can guide the experimental operation of droplet suspension. To successfully hang a droplet on the suspender, initial state of the droplet should be carefully controlled so that the transition from the initial state to the steady state can be as smooth as possible, which is especially true for non-wettable surfaces.

References

Adam, N.K., Livingston, H.K., 1958. Contact angle and work of adhesion. Nature 182, 128.

Al Zaitone, B., Al-Zahrani, A., Al-Shahrani, S., Lamprecht, A., 2020. Drying of a single droplet of dextrin: Drying kinetics modeling and particle formation. Int. J. Pharm. 574, 118888.

Archer, J., Walker, J.S., Gregson, F.K., Hardy, D.A., Reid, J.P., 2020. Drying kinetics and particle formation from dilute colloidal suspensions in aerosol droplets. Langmuir 36, 12481–12493.

Bansal, L., Seth, P., Sahoo, S., Mukherjee, R., Basu, S., 2018. Beyond coffee ring: Anomalous self-assembly in evaporating nanofluid droplet on a sticky biomimetic substrate. Appl. Phys. Lett. 113, 213701.

Baumann, J.M., Adam, M.S., Wood, J.D., 2021. Engineering advances in spray drying for pharmaceuticals. Annual Review of Chemical and Biomolecular Engineering 12, 217–240.

Bhardwaj, R., Agrawal, A., 2020. Tailoring surface wettability to reduce chances of infection of COVID-19 by a respiratory droplet and to improve the effectiveness of personal protection equipment. Phys. Fluids 32, 081702.

Bond, W., 1935. The surface tension of a moving water sheet. Proceedings of the Physical Society (1926-1948) 47, 549.

Both, E., Siemons, I., Boom, R., Schutyser, M., 2019. The role of viscosity in morphology development during single droplet drying. Food Hydrocoll. 94, 510–518.

Both, E., Boom, R., Schutyser, M., 2020. Particle morphology and powder properties during spray drying of maltodextrin and whey protein mixtures. Powder Technol. 363, 519–524.

Brackbill, J.U., Kothe, D.B., Zemach, C., 1992. A continuum method for modeling surface tension. J. Comput. Phys. 100, 335–354.

Charlesworth, D., Marshall Jr, W., 1960. Evaporation from drops containing dissolved solids. AIChE J 6, 9–23.

Chaudhuri, S., Basu, S., Kabi, P., Unni, V.R., Saha, A., 2020. Modeling the role of respiratory droplets in Covid-19 type pandemics. Phys. Fluids 32, 063309.

Chauveau, C., Birouk, M., Gökalp, I., 2011. An analysis of the d2-law departure during droplet evaporation in microgravity. Int. J. Multiph. Flow 37, 252–259.

Dang, Q., Song, M., Zhang, X., Pekař, L., Hosseini, S.H., 2022. Modelling study on freezing process of water droplet on inclined cold plate surface with droplet dynamic behavior considered. Int. J. Heat Mass Transf. 197, 123327.

de Souza Lima, R., Ré, M.-I., Arlabosse, P., 2020. Drying droplet as a template for solid formation: A review. Powder Technol. 359, 161–171.

Deegan, R.D., Bakajin, O., Dupont, T.F., Huber, G., Nagel, S.R., Witten, T.A., 1997. Capillary flow as the cause of ring stains from dried liquid drops. Nature 389, 827–829.

Eijkelboom, N.M., van Boven, A.P., Siemons, I., Wilms, P.F., Boom, R.M., Kohlus, R., Schutyser, M.A., 2022. Particle structure development during spray drying from a single droplet to pilot-scale perspective. J. Food Eng. 337, 111222.

Filková, I., Mujumdar, A.S., 2020. Industrial spray drying systems. Handbook of Industrial Drying 263–307.

Fu, N., Woo, M.W., Chen, X.D., 2011. Colloidal transport phenomena of milk components during convective droplet drying. Colloids Surf. B Biointerfaces 87, 255–266.

Fu, N., Woo, M.W., Chen, X.D., 2012. Single droplet drying technique to study drying kinetics measurement and particle functionality: a review. Drying Technol. 30, 1771–1785.

George, O.A., Xiao, J., Rodrigo, C.S., Mercadé-Prieto, R., Sempere, J., Chen, X.D., 2017. Detailed numerical analysis of evaporation of a micrometer water droplet suspended on a glass fila-ment. Chem. Eng. Sci. 165, 33–47.

George, O.A., Xiao, J., Mercadé-Prieto, R., Fu, N., Chen, X.D., 2019. Numerical probing of suspended lactose droplet drying experiment. J. Food Eng. 254, 51–63.

Ghata, N., Shaw, B.D., 2014. Computational modeling of the effects of support fibers on evaporation of fiber-supported droplets in reduced gravity. Int. J. Heat Mass Transf. 77, 22–36.

Ghauri, S.A., Ansari, M.S., 2006. Increase of water viscosity under the influence of magnetic field. J. Appl. Phys. 100, 066101.

Gregson, F., Robinson, J., Miles, R., Royall, C., Reid, J., 2018. Drying kinetics of salt solution droplets: Water evaporation rates and crystallization. J. Phys. Chem. B 123, 266–276.

Groenewold, C., Möser, C., Groenewold, H., Tsotsas, E., 2002. Determination of single-particle drying kinetics in an acoustic levitator. Chem. Eng. J. 86, 217–222.

Huang, L., Liu, Z., Liu, Y., Gou, Y., Wang, L., 2012. Effect of contact angle on water droplet freezing process on a cold flat surface. Exp. Therm Fluid Sci. 40, 74–80.

Khattab, I.S., Bandarkar, F., Fakhree, M.A.A., Jouyban, A., 2012. Density, viscosity, and surface tension of water+ ethanol mixtures from 293 to 323K. Korean J. Chem. Eng. 29, 812–817.
Kristensen, D., Jensen, P.Y., Madsen, F., Birdi, K.S., 1997. Rheology and surface tension of selected processed dairy fluids: Influence of temperature. J. Dairy Sci. 80, 2282–2290.
Langstaff, D., Gunn, M., Greaves, G., Marsing, A., Kargl, F., 2013. Aerodynamic levitator furnace for measuring thermophysical properties of refractory liquids. Rev. Sci. Instrum. 84, 124901.
Larson, R.G., 2017. Twenty years of drying droplets. Nature 550, 466–467.
Lin, S.X.Q., Chen, X.D., 2002. Improving the glass-filament method for accurate measurement of drying kinetics of liquid droplets. Chem. Eng. Res. Des. 80, 401–410.
Littringer, E., Paus, R., Mescher, A., Schroettner, H., Walzel, P., Urbanetz, N., 2013. The morphology of spray dried mannitol particles—The vital importance of droplet size. Powder Technol. 239, 162–174.
Liu, H.-J., Kang, Y., 2006. Regulating field microclimate using sprinkler misting under hot-dry windy conditions. Biosyst. Eng. 95, 349–358.
Meng, X., Meng, L., Gao, Y., Li, H., 2022. A comprehensive review on the spray cooling system employed to improve the summer thermal environment: Application efficiency, impact factors, and performance improvement. Build. Environ. 217, 109065.
Mittal, R., Ni, R., Seo, J.-H., 2020. The flow physics of COVID-19. J. Fluid Mech. 894, F2.
Paria, S., Biswal, N.R., Chaudhuri, R.G., 2015. Surface tension, adsorption, and wetting behaviors of natural surfactants on a PTFE surface. AIChE J 61, 655–663.
Perdana, J., Fox, M.B., Schutyser, M.A.I., Boom, R.M., 2013. Mimicking spray drying by drying of Single Droplets Deposited on a Flat Surface. Food Bioproc. Tech. 6, 964–977.
Piñón-Balderrama, C.I., Leyva-Porras, C., Terán-Figueroa, Y., Espinosa-Solís, V., Álvarez-Salas, C., Saavedra-Leos, M.Z., 2020. Encapsulation of active ingredients in food industry by spray-drying and nano spray-drying technologies. Processes 8, 889.
Radhakrishnan, S., Srivathsan, N., Anand, T., Bakshi, S., 2019. Influence of the suspender in evaporating pendant droplets. Int. J. Therm. Sci. 140, 368–376.
Raghavan, V., Mehta, P.S., 2015. Vaporization characteristics of suspended droplets of biodiesel fuels of Indian origin and their diesel blends–An experimental study. Int. J. Heat Mass Transf. 88, 28–41.
Rehman, H.L., Weiss, J., Seers, P., 2016. Effect of heat conduction on droplet life time and evaporation rate under forced convection at low temperatures. Exp. Therm Fluid Sci. 72, 59–66.
Rosli, M.A., Aziz, A.R.A., Ismael, M.A., Elbashir, N.O., Baharom, M., Mohammed, S.E., 2021. Experimental study of micro-explosion and puffing of gas-to-liquid (GTL) fuel blends by suspended droplet method. Energy 218, 119462.
Rosti, M., Olivieri, S., Cavaiola, M., Seminara, A., Mazzino, A., 2020. Fluid dynamics of COVID-19 airborne infection suggests urgent data for a scientific design of social distancing. Sci. Rep. 10, 1–9.
Saad, S.M.I., Neumann, A.W., 2016. Axisymmetric drop shape analysis (ADSA): An outline. Adv. Colloid Interface Sci. 238, 62–87.
Saha, A., Basu, S., Kumar, R., 2012. Particle image velocimetry and infrared thermography in a levitated droplet with nanosilica suspensions. Exp. Fluids 52, 795–807.
Shih, A.T., Megaridis, C.M., 1995. Suspended droplet evaporation modeling in a laminar convective environment. Combust. Flame 102, 256–270.
Sobac, B., Brutin, D., 2011. Triple-line behavior and wettability controlled by nanocoated substrates: influence on sessile drop evaporation. Langmuir 27, 14999–15007.
Solanki, G., Rizvi, S.S.H., 2001. Physico-Chemical properties of skim milk retentates from microfiltration. J. Dairy Sci. 84, 2381–2391.
Su, Y., Fu, N., Xiao, J., Chen, X.D., 2020. Vaporization and particle formation during drying of multisolvent droplet without and with antisolvent-vapor infusion. Chem. Eng. Sci. 219, 115617.
Surendran, M., Anand, T., Bakshi, S., 2020. Experimental investigation of the evaporation behavior of urea-water-solution droplets exposed to a hot air stream. AIChE J 66, e16845.
Tadmor, R., Das, R., Gulec, S., Liu, J.E., N'guessan, H., Shah, M.S., Wasnik, P., Yadav, S. B., 2017. Solid–liquid work of adhesion. Langmuir 33, 3594–3600.
Tan, Q., Yang, A., Guo, P., 2019. Blind modulation format identification using differential phase and amplitude ratio. IEEE Photonics J. 11, 1–12.
Tong, W.L., Tan, M.K., Chin, J.K., Ong, K.S., Hung, Y.M., 2015. Coupled effects of hydrophobic layer and vibration on thermal efficiency of two-phase closed thermosyphons. RSC Adv. 5, 10332–10340.
Vargaftik, N., Volkov, B., Voljak, L., 1983. International tables of the surface tension of water. J. Phys. Chem. Ref. Data 12, 817–820.
Vershinina, K.Y., Egorov, R.I., Strizhak, P.A., 2016. The ignition parameters of the coal-water slurry droplets at the different methods of injection into the hot oxidant flow. Appl. Therm. Eng. 107, 10–20.
Volkov, R., Strizhak, P., 2021. Using Planar Laser Induced Fluorescence and Micro Particle Image Velocimetry to study the heating of a droplet with different tracers and schemes of attaching it on a holder. Int. J. Therm. Sci. 159, 106603.
Weber, J., Tamalonis, A., Benmore, C., Alderman, O., Sendelbach, S., Hebden, A., Williamson, M., 2016. Aerodynamic levitator for in situ x-ray structure measurements on high temperature and molten nuclear fuel materials. Rev. Sci. Instrum. 87, 073902.
Wen, X., Wang, M., Su, T., Zhang, S., Pan, R., Ji, W., 2019. Suppression effects of ultrafine water mist on hydrogen/methane mixture explosion in an obstructed chamber. Int. J. Hydrogen Energy 44, 32332–32342.
Wu, W.D., Patel, K.C., Rogers, S., Chen, X.D., 2007. Monodisperse droplet generators as potential atomizers for spray drying technology. Drying Technol. 25, 1907–1916.
Wu, W.D., Amelia, R., Hao, N., Selomulya, C., Zhao, D., Chiu, Y.L., Chen, X.D., 2011. Assembly of uniform photoluminescent microcomposites using a novel micro-fluidic-jet-spray-dryer. AIChE J 57, 2726–2737.
Yarin, A.L., Brenn, G., Rensink, D., 2002. Evaporation of acoustically levitated droplets of binary liquid mixtures. Int. J. Heat Fluid Flow 23, 471–486.
Zandona, A., Martinez Arias, A., Gutbrod, M., Helsch, G., Weber, A.P., Deubener, J., 2021. Spray-Dried TiO2 (B)-Containing photocatalytic glass-Ceramic nanobeads. Adv. Funct. Mater. 31, 2007760.
Zang, D., Tarafdar, S., Tarasevich, Y.Y., Choudhury, M.D., Dutta, T., 2019. Evaporation of a droplet: from physics to applications. Phys. Rep. 804, 1–56.
Zhang, Y., Matthews, S., Tran, A.T.T., Hyland, M., 2016. Effects of interfacial heat transfer, surface tension and contact angle on the formation of plasma-sprayed droplets through simulation study. Surf. Coat. Technol. 307, 807–816.